

# Computer simulations of sample chambers for laser ablation–inductively coupled plasma spectrometry

Davide Bleiner<sup>\*</sup>, Annemie Bogaerts

University of Antwerp, Department of Chemistry, Research Group for Plasma, Laser Ablation & Surface Modelling - Antwerp (PLASMANT), Belgium

Received 25 September 2006; accepted 15 February 2007

Available online 27 February 2007

## Abstract

The performance of several sample chambers was studied by means of computational fluid dynamics. The geometry and size was found to influence the gas velocity pattern as well as the extraction efficiency. The extraction efficiency of *conventional* ‘drum-shaped’ cells, in the volume range 3 to 100 cm<sup>3</sup>, was between 5 and 15% (number of particles), depending on the size and operating conditions such as gas flow rate, type of carrier gas. *Optimized* designs permitted as high as factor of six improved extraction efficiency. The use of helium improved the transport *speed* and extraction *reproducibility* of large volume cell. However, Ar showed better extraction *efficiency* than He, especially for the finer particles, due to a shorter mean free path, which mitigated nano-particle slipping.

© 2007 Elsevier B.V. All rights reserved.

**Keywords:** Laser ablation cell; Sample chamber modelling; Transport efficiency

## 1. Introduction

Direct solid micro-analysis using laser ablation (LA) in combination with inductively coupled plasma (ICP) mass spectrometry (MS) has been successfully implemented in several applications, e.g., in the geo-sciences, material sciences, bio-sciences, forensic, art, and cultural heritage [1,2]. During the LA–ICP–MS measurement, the sample chamber (or ablation cell) plays an important role, because (i) it should permit a *quantitative* transport of the laser-induced aerosol, and because (ii) it should lead to a *rapid* transport from the ablation site to the ICP source.

‘Quantitative transport’ means that the ablation cell should minimize aerosol loss. Mass conservation during *entrainment* (i.e. to draw in and transport all solid particles by the flow of the fluid [3]) is important to obtain high signal-to-noise ratios (SNR), low detection limits (DL) as well as for avoiding biased particle transport, leading to elemental fractionation. On the other hand, ‘rapid aerosol entrainment’ is also important, in order to minimize signal dispersion, particle residence time in

the cell, particle–particle or particle–wall reaction, and the tailing of LA–ICPMS signals [4].

Moenke-Blankenburg and co-workers [5–7] reviewed the evolution of laser ablation cell design, and discussed the performance in LA–ICP optical emission spectrometry (OES), showing that advantages and disadvantages combine together in any designs. Concerning the figures of merit, it should be pointed out that in the 1980s the user had to acquire all the information simultaneously from the ablation of one single laser pulse, due to laser hardware limitations. Therefore, pulse-to-pulse statistics played a significant role, a consideration that has gradually demoted in recent times because of the availability of high repetition rate commercial systems, with better than 5% stability. In general, ‘statistics’ is due to both the laser-energy fluctuations and the set-up-related fluctuations in aerosol flush efficiency. Therefore, considering the significant improvement of the laser hardware, nowadays the major challenge for improving LA–ICPMS signal characteristics is quite on the aerosol-entrainment and transport stage than on the sampling.

The ablation cells can be schematically divided into two groups, i.e., the *open design* and the *closed design* ablation cells. Open designs are those cells juxtaposed upon a sample surface that must be polished and smooth for optimized sealing,

<sup>\*</sup> Corresponding author. Universiteitsplein 1, 2610 Antwerp, Belgium.

E-mail address: [davide.bleiner@ua.ac.be](mailto:davide.bleiner@ua.ac.be) (D. Bleiner).

so enclosing the volume above the irradiated surface. These cells permit to minimize dead volume even in combination with large samples. On the other hand, the closed design cells are the more conventional “box-like” cells enclosing the entire sample(s). These cells do not demand the sample to be previously polished, but the sample must match specific size restrictions to fit in. Unfortunately, such sample chambers induce signal dispersion as a function of increasing size. Presently, this is the most widely used ablation cell type (cfr. *Cetac*<sup>®</sup>, *New Wave Research*<sup>®</sup>), especially the cylindrical one, where in order to accommodate more targets (samples or reference materials) one has to scale-up the total cell volume. Increased volume enhances signal dispersion as well as the possibility of aerosol loss by gravitation in regions of low flush efficiency [8]. The flow pattern across the chamber can change significantly as a consequence of modified cell characteristics, i.e., volume, shape, number of inlets, materials etc.

### 1.1. Chamber designs

Several workers have tried to develop novel and better designs of ablation cells to accomplish better figures of merits in LA–ICPMS (see Table 1). The guiding criteria were maximization of both aerosol *extraction efficiency* and *transport speed*. Here, we summarize the most significant achievements following a chronological order within the above explained subdivision in two main logical groups.

#### 1.1.1. Open cells

Already in the mid and late 1970s, a number of authors [9,10] designed open design LA cells for flame atomic absorption spectrometry or microwave discharges. At the beginning of the 1980s, Carr and Horlick [11] developed an open design for ICP spectrometry composed by a sample-clamping swivel vice. The ablation cell could be connected to the bottom of an ICP torch with a standard ball joint. The ablation volume was a cylinder of few cm<sup>3</sup>, with the axial direction parallel to the laser beam. The sample was a disc that should meet certain size requirements because it sealed one edge of the cell. Ishizuka and Uwamino [12], in order to allow more flexibility with the mounting of the sample, preferred the use of remote ablation cells connected via plastic tubing to the

sample inlet of an ICP. The cell size was a compromise between signal dispersion and minimization of aerosol spattering on the walls (so-called *wall reaction*), which is enhanced in reduced size cells. Thompson et al. [13] also adopted this approach of remote connection of the sample chamber to the ICP via tubing, yet in combination with a closed-design ablation cell.

#### 1.1.2. Closed cells

Dittrich and Wennrich [14] introduced the first sample chamber fully enclosing the sample(s), with the advantages that the ablation could be performed with no sample preparation such as surface polishing, and at atmospheric pressure that permitted the direct analysis of pressed pellets, clearly unstable under vacuum conditions. In the milestone paper by Gray [15], who was the first one to couple LA to ICP Mass Spectrometry (MS), the sample cell was a 130 cm<sup>3</sup> cylindrical cell with inlet and outlet at different elevations and movable sample stage to match the sample surface position with the gas inlet level. The laser, transmitted through a borosilicate glass window that topped the cell, irradiated the target at 90° (i.e. normal to the surface). The gas inlet was feeding tangentially the ablation cell, so that a swirling motion over the surface was produced and the laser-induced aerosol was entrained orthogonally to the ablation direction. Unfortunately, this influenced the probability of particle–wall reaction, aerosol dispersion, and signal tailing. Although a similar principle had already been applied in Ref. [11], it should be said that wall reaction effects were in that case not so pronounced because having the ablation cell directly feeding the ICP torch mitigated any risk aerosol dispersion. Mitchell et al. [16] presented a closed sample chamber for solid analysis using LA combined to DC plasma spectrometry. It consisted of two major parts: the motorized sample platform and the aluminum body with a lens as the laser focusing unit.

Quite original designs were then introduced as concerns on the carrier gas flow dynamics became an issue, beyond mere ‘sample holding’ requirements. Arrowsmith [17] designed a “bottle-shaped” chamber connected to the ICP via plastic tubing from the bottleneck. The target was located at the “bottle-floor” and could be irradiated at an angle of 50–60° off-normal. In this design, the aerosol entrainment was coaxial with the ablation of particles, which suggested improved transport. A further innovation was the *tilted beam approach*, which reduced laser

Table 1  
List of laser ablation cells in the literature and their main characteristics

Ref.	Year	Description
Kantor [9]	1976	Designed for flame AAS
Dittrich and Wennrich [14]	1980	Designed as closed system to avoid sample preparation (polishing)
Thompson et al. [13]	1981	Remote cell connected to the ICP via PVC tubing
Carr and Horlick [11]	1982	Designed to fit ICP torch tail
Ishizuka and Uwamino [12]	1982	Cap cell for polished surfaces (Aufsatz design)
Gray [15]	2002	Cylindrical with tangential Ar inlet and adjustable sample height
Arrowsmith [17]	1987	Bottle-shaped design with ablation direction parallel to gas flow
Arrowsmith [19]	1988	Design with variable possible combination of gas flow inlet/outlet
Mitchell et al. [16]	1985	Designed for DCP spectrometry
Su and Lin [21]	1986	Type I: standard cylindrical with symmetry axis normal to flow axis. Type II: bottle-shaped with tangential Ar introduction
Gäckle and Güenther [7]	1988	Designed to fit into a petrographic microscope in the laser system
Bleiner [23]	1990	Gun barrel: designed to minimize volume with many samples per run Piston cell: designed for flexible cell volume adjustment

plume-shielding and possibly minimized molten droplet splashing, according to what was reported in Ref. [18]. Arrowsmith and Hughes [19] tested also a hybrid setup made of an open-design cell nested inside a outer box, which has been recently adopted also by Garcia et al. [20]. The outer cell was always kept fixed, like the optics and the beamline, and the sample was moved by means of stepper motors. Depending on the type of inner cell mounted, the gas could flow into the ablation volume leaking through the floor contact and flowing in from the topside (a), leaking through the floor contact and closing the topside with a window (b), or alternatively through a feeding tubing line (c). The first and second cells showed fast rising and falling signal edges, but also strong particle–wall reaction, which significantly extended the rinse time to several minutes, also due to reentry of particles which escaped from the cell and mixed with the gas in the outer box.

The popular “drum-like” design, with inlet/outlet located on the sides, and a glass window as the top face, was then introduced and mastered the market. The reason of the success of such a design, we believe, is to be attributed to the *simplicity of construction* (the machine workshop’s task essentially limits to fixing a threaded cylinder on a slab), the *flexibility* for number of targets to be processed per measurement session – though neglecting issues of cross-contamination and flow dynamics – and also some *lack of innovation* drive on the side of the manufacturers. Unfortunately, after the appropriate optimizations reported by Arrowsmith and co-workers [17,19], the *drum* design represents a step back, considering the lack of attention for the gas flow dynamics, as also evident from the results of Su and Lin [21]. They designed and tested two types of closed-design ablation cells, i.e., a standard *drum* cell and again a *bottle* cell. The experimental results indicated that the bottle-shaped cell provided more than one order of magnitude improved sensitivity and much better detection limits across the mass spectrum. The authors explained the results qualitatively with the different flow pattern across the two ablation cells, which significantly enhanced transport characteristics. A certain correction of this negative trend was presented in Cousin and Magyar [22]. In fact, a whirlpool was induced in a *drum* ablation cell to steer the laser-induced aerosol fluid—dynamically into the transport tubing. To do so, the gas inlet was off-axis with the outlet, at an angle of 60° and the outlet being a few cm’s above the inlet plane, to favor vorticity. Bleiner and Günther [8,23] developed an original design that combined small signal dispersion, no-cross contamination, and multi-sample capability. This was obtained with a so-called “gun-barrel” approach: only the target to be ablated was brought inside the ablation volume, rotating the sample holder disc, similarly like the barrel of a revolver. Thus, the samples remained separated, which helped to avoid cross-contamination, many samples could be analyzed during the same measurement session, and the laser-induced aerosol was rapidly entrained (individual single shot signals were five times sharper and four times higher than in a 60 cm<sup>3</sup> drum cell). The ablation volume was shaped like a half ellipse with the inlet on the flat face, directly facing the outlet on the apex of the curved face. Nevertheless, the wash-out time was degraded, possibly due to a

more relevant particle–wall reaction, which is typical of small volume chambers. Bleiner [23] also designed a so-called “piston cell”, realized from a plastic syringe of 50 cm<sup>3</sup>. The advantage of that cell design was the possibility to flexibly modify the chamber volume, and thus modulate the LA–ICPMS signal profile according to the ICP–MS acquisition speed, and avoid spectral skew [24] in LA–ICPMS with sector field instruments. Moreover, the plug flow ensured better transport conditions.

### 1.2. Optimization studies

Concerning the analytical performance, Gäckle and Günther [7] made the first experimental study on the influence of ablation set-up on signal characteristics in combination with ICP–OES, showing that the volume of the ablation cell represented the most limiting factor in terms of signal dispersion. They investigated both open and closed cell designs and pointed out another important characteristic of open cell designs, namely that the laser focal distance has to be fixed. In fact, the laser-focusing lens must be selected to match the height of the cell, and does not allow choosing the most appropriate optics for a given application, i.e., lateral vs. depth resolution. Another novel approach, used in combination with the closed design was the implementation of an inlet needle, in order to ensure a high gas flow velocity. In several works by the ETH group [8,23] it was shown that the use of a gas inlet needle in a closed design ablation cell favors the formation of a gas jet at the nozzle tip. Hence, a high transport efficiency region was observed in front of the nozzle tip, whereas marginal portions of the ablation cell were characterized by low flush efficiency. When the laser was focused on the sample surface within the cell’s high efficiency region, higher signal intensity was obtained compared to operation with no nozzle at all. Yet, the variability of signal intensity obtained from the ablation of the same sample in different positions across the ablation cell was large (30–40% signal fluctuations when using Ar, or 10% when using He).

Pisonero et al. [25] have recently introduced a novel concept of LA sample chamber, based on a *gas-drawing effect* at the outlet, as opposed to the traditional *gas-pushing effect* at the inlet. The performance of the experimental system is fully documented in the original article, and any comparison with the results shown in the present paper would not be appropriate, since we are basing our modelling work on the traditional concept.

### 1.3. Rationale of simulation study

Aim of the present study was to investigate the fluid-dynamic characteristics of laser ablation chambers from theoretical principles. This was done by means of computational fluid dynamics (CFD), in order to evaluate the impact of several design and operating characteristics on the entrainment and transport speed of laser-induced aerosol. Section 2 describes the model and its mathematical features. Section 3 is dedicated to the numerical simulation results, focusing on the

extraction efficiency and speed, as obtained from in-cell pressure distribution, flow velocity pattern and particle trajectories. For these studies, standard cylindrical ablation cells were initially simulated and later on their characteristics were gradually optimized. As a matter of fact, although the cylindrical cell is not necessarily the best one, it is rather popular. Hence, it is very useful to be used as a starting benchmark for many readers familiar with LA–ICPMS.

## 2. The computational model

### 2.1. Numerical treatment

The *Gambit/Fluent* modelling package was used for developing our CFD simulations. The first step of the model development was building-up the *pre-processor*, i.e., defining the geometry of the sample chamber body and then meshing it as a numerical network. The meshing scheme used led to a tetragonal network. The size of the cells was adapted to cover homogeneously the whole chamber body, with a denser network at locations where more detailed solutions were needed, such as the gas inlet/outlet and the walls. The second step was the implementation of the *solver*. A finite volume algorithm was used to solve the set of differential equations within each 3D mesh cell, which guarantee optimal conservation. A coupled implicit scheme was adopted for 2000 iterations (*Courant number* equal to 1), followed by a segregated implicit scheme which led to faster convergence, with residuals better than  $10^{-5}$ .

### 2.2. Governing equations

The governing equations were obtained from conservation of mass (Eq. (1)) and momentum (Eq. (2)), namely:

$$\frac{d\rho}{dt} + \nabla \cdot (\rho \vec{v}) = S_m \quad (1)$$

$$\frac{d\rho \vec{v}}{dt} + \nabla \cdot (\rho \vec{v} \vec{v}) = -\nabla \vec{p} + \nabla \cdot \vec{\tau} + \rho \vec{g} \quad (2)$$

where  $\rho$  is the mass density,  $\vec{v}$  is the velocity,  $\vec{p}$  is pressure,  $\vec{g}$  is the gravity acceleration. Additional body forces acting on the momentum of the particles or the fluid were accounted too, as explained in detail elsewhere [26]. The source/sink term  $S_m$  is the mass added during the ablation and lost from the cell in the extraction. The stress tensor  $\vec{\tau}$  is a function of the molecular viscosity  $\mu$  as given explicitly by the following equation:

$$\vec{\tau} = \mu \left[ (\nabla \vec{v} + \nabla \vec{v}^T) - \frac{2}{3} \nabla \cdot \vec{v} I \right] \quad (3)$$

where  $\vec{v}^T$  is the transposed velocity vector, and  $I$  is the identity matrix. Since processes of heat transfer or compressibility (shock wave) were not involved, the energy conservation equation had not to be implemented (thermal equilibrium). However, two more governing equations had to be solved, in

order to account for viscous turbulence. Turbulence was described using a so-called *realizable*  $k - \epsilon$  model [27,28], which is the most widely-used two-equation eddy-viscosity turbulence model. The *realizable* version of the  $k - \epsilon$  model is a recent advance and modification, which satisfies certain mathematical constraints on the Reynolds stresses, consistent with the physics of rapid inlet flows, and which more accurately predicts the spreading rate of jets. Further mathematical and physical details can be found in the original papers by Harlow and Nakayama as well as Launder and Spalding [27,28].

### 2.3. Extraction rate

The aerosol extraction from the chamber can be quantitatively expressed as the *collision rate* of the LA-induced particles with the cell outlet. The extraction rate ( $v_{\text{coll}}$ ) is thus the product of outlet cross-section ( $\sigma_{\text{out}}$ ), the particle number density ( $n_p$ ), and the particle velocity ( $v_p$ ), namely:

$$v_{\text{coll}} = \sigma_{\text{out}} n_p v_p \quad (4)$$

Hence, the extraction rate as given in Eq. (4) has the units of counts per second (cps or  $s^{-1}$ ), and quantifies the number of particles escaping through the outlet gate per unit of time. The first parameter in the given expression, the *outlet cross-section*, shows that the extraction efficiency increases with the diameter of the outlet. This definition considers that the size of the various particles is much smaller than the outlet itself, and thus can be treated as points, whose collision with the outlet is determined by the outlet cross-section only. The second parameter, *the particle number density*, is the ratio between number of free particles in the chamber ( $N$ ) and the volume of the chamber ( $V$ ). At a fixed number of ablated particles, large ablation cells, where the number density is proportionally lower, have reduced extraction efficiency because of higher dispersion, so that the probability that a particle “flies-by” and “hits” the outlet decreases. On the other hand, for a given constant cell volume, the higher the number of particles, the higher the evacuation probability, due to improved hit counting statistics. The third parameter determining the extraction rate is the *velocity of the particles*, which is influenced by the flow pattern across the cell. Clearly, the faster a particle moves, the higher the hit rate with the outlet gate in a given time. If the velocity becomes zero, i.e., the particle settles-down inside the cell, the probability for that particle to leave the cell becomes also zero. Besides an apparently obvious statement, the latter sentence expresses the fact that the transport efficiency of a cell should be determined over long observation periods. In fact, as long as a particle is “loft” in the gas mass, there is a non-zero chance that it might exit from the cell at a certain instant. If the cell is large this event might require a proportionally longer period of time, of the order of several seconds or even more. Due to the obvious fact that particle trajectory calculations cannot be performed over an infinite length, in our simulations we tracked the trajectories of individual particles for as long as 50 m. All particle trajectories that were longer than such *cutoff length* were aborted and not computed any further. Such particles were

thus trapped inside the chamber. Hence, the extraction efficiency values obtained and reported in Table 2 refer to the particles *escaped* from the chamber prior the cutoff length was attained. It should be also pointed out that the extraction rates obtained in this work are given as *number of particles*, i.e. regardless of their size, whereas in terms of mass extraction efficiency, as often found in the literature [20], the *micro-sized fraction* would give a more significant contribution than the fine *nano-sized fraction*.

#### 2.4. Computational conditions

The discrete phase was a particle ensemble of Cu with characteristics matched to fourth-harmonic (266 nm) Nd:YAG ns-pulse laser ablation, as investigated previously [29]. Comparisons with studies based on fs-pulse laser ablation such as in Ref. [20] would be unfair, because the particle size distribution produced under ultra-short pulse irradiation is known to be much finer, which affects the aerosol extraction efficiency, too. The minimum particle diameter was here 10 nm, the maximum was 10  $\mu\text{m}$ , and the mean size was 20 nm, which was experimentally derived from differential mobility analyzer measurements on ablated brass [29]. For the current simulations, the particle size distribution was divided into 10 channels. The mass production rate, as a consequence of pulsed laser ablation, was  $3 \cdot 10^{-10}$  kg/s, which was calculated considering 10 Hz repetition rate, with an ablated mass per shot of 30 ng/pulse (this value was experimentally determined in Ref. [30]). As a boundary condition, the gas inlet was set to a *gauge* pressure of 13.5 kPa (i.e. 1 L/min for our geometry). However, when specific calculations required to reduce the inlet flow (e.g., see part on multi-inlet cells, or flow rate effects), this value was modified according to the Hagen–Poiseuille law [31] to relate input pressure and gas flow. A further boundary condition refers to the elements of the computational model, namely the kind of interaction cell–solid particles. With respect to this

point, the *walls* were set as reflecting barriers, the *outlet* as escape gate, the *inlet* as input source.

Parameter distributions were initially calculated for three cylindrical ablation cells of respective volumes 2.7 cm<sup>3</sup>, 33.7 cm<sup>3</sup>, and 98.2 cm<sup>3</sup>. Then, the performance was optimized in a second stage modifying the design, and the operating conditions. Table 2 summarizes characteristics and results of all simulated models.

### 3. Results and discussion

#### 3.1. Gas velocity pattern

Fig. 1 summarizes calculated gas velocity distributions as a function of chamber volume. For the 2.7 cm<sup>3</sup> cell in panel (a) the flow pattern is characterized by a fast rotational motion, due to the spatial confinement of the inlet jet. The asymmetry in the gas speed magnitude is a transient situation related to the chaotic evolution of the flow pattern. The spin direction in the left and right-hand subzones is opposite, i.e., clockwise for the right-hand one (bottom of Fig. 1.a1) and counter-clockwise for the left-hand one (top of Fig. 1.a1). The motion of the gas is in both the left and right margin of the cell retrograde, i.e., the gas moves backward to compensate the forward flow along the inlet–outlet axis.

For the 33.7 cm<sup>3</sup> cell in panel (b) the flow pattern is confined by a slight static pressure increase. The latter limits significantly the forward expansion of the gas inlet plume. The geometry of the gas plume is compressed along the forward direction and expanded laterally, so to give a sub-spherical shape. A remarkable character is the strong vorticity coupled back on the gas plume expansion. The flow through the outlet, shows a more regular axi-symmetric parabolic profile.

For the 98.2 cm<sup>3</sup> ablation cell in panel (c) the static pressure is modestly above the atmospheric pressure. The most evident effect of this situation is that the gas plume expands for almost the entire diameter of the ablation cell. However, outside of the gas plume length, which could be considered as the *high-efficiency transport region* of Ref. [8], the gas moves significantly slower (low-efficiency transport area). Local fluctuations of the gas flow pattern can induce a transient lateral tilt of the gas plume axis. All samples that are ablated in off-axis positions across the cell would consequently provide more modest and erratic sensitivity, also considering the fact that the gas flow lines point backward. Hence, in large ablation cells, aerosol recirculation is a severe problem that causes transport delay, signal tailing and sample cross-contamination.

#### 3.2. Particle trajectories and extraction efficiency

Fig. 2 summarizes calculated particle trajectories as a function of particle size, in the range 10 nm–10  $\mu\text{m}$ . Table 2 summarizes obtained values of the extraction efficiency for the various cell designs simulated. As a general comment, fine particles followed more complicated trajectories, due to the Brownian motion, and there is a high chance that they might not reach the outlet within the 50 m *cut-off* distance, which reduces their extraction

Table 2  
List of laser ablation cells simulated in this study, their main characteristics, and calculated extraction efficiency

Chamber	Volume (cm <sup>3</sup> )	Gas flow (L/min)	Efficiency (%)	RSD (%)
Drum, AR=1	2.7	Ar=1.0	4.8	4.2
	33.7		10.1	2.2
	33.7	Ar=0.5	15.4	3.0
	33.7	Ar=0.1	5.7	2.8
	33.7	He=1.0	11.4	4.1
	33.7	He=0.5	14.4	0.5
	98.2	Ar=1.0	9.9	1.3
Drum, AR=0.25	32.7	Ar=1.0	15.7	0.8
	32.3	Ar=1.0	8.7	2.4
Drum, AR=0.5	32.6	Ar=1.0	3.8	17.0
Drum, AR=4	32.1	Ar=1.0	25.2	1.0
Elliptical	24.6	Ar=1.0	10.1	0.1
Pyramidal front	33.7	Ar=1.0	65.9	0.2
Piston	33.7	He=1.0	52.9	0.6

<sup>a</sup>AR' is the aspect ratio of vertical cross-section.

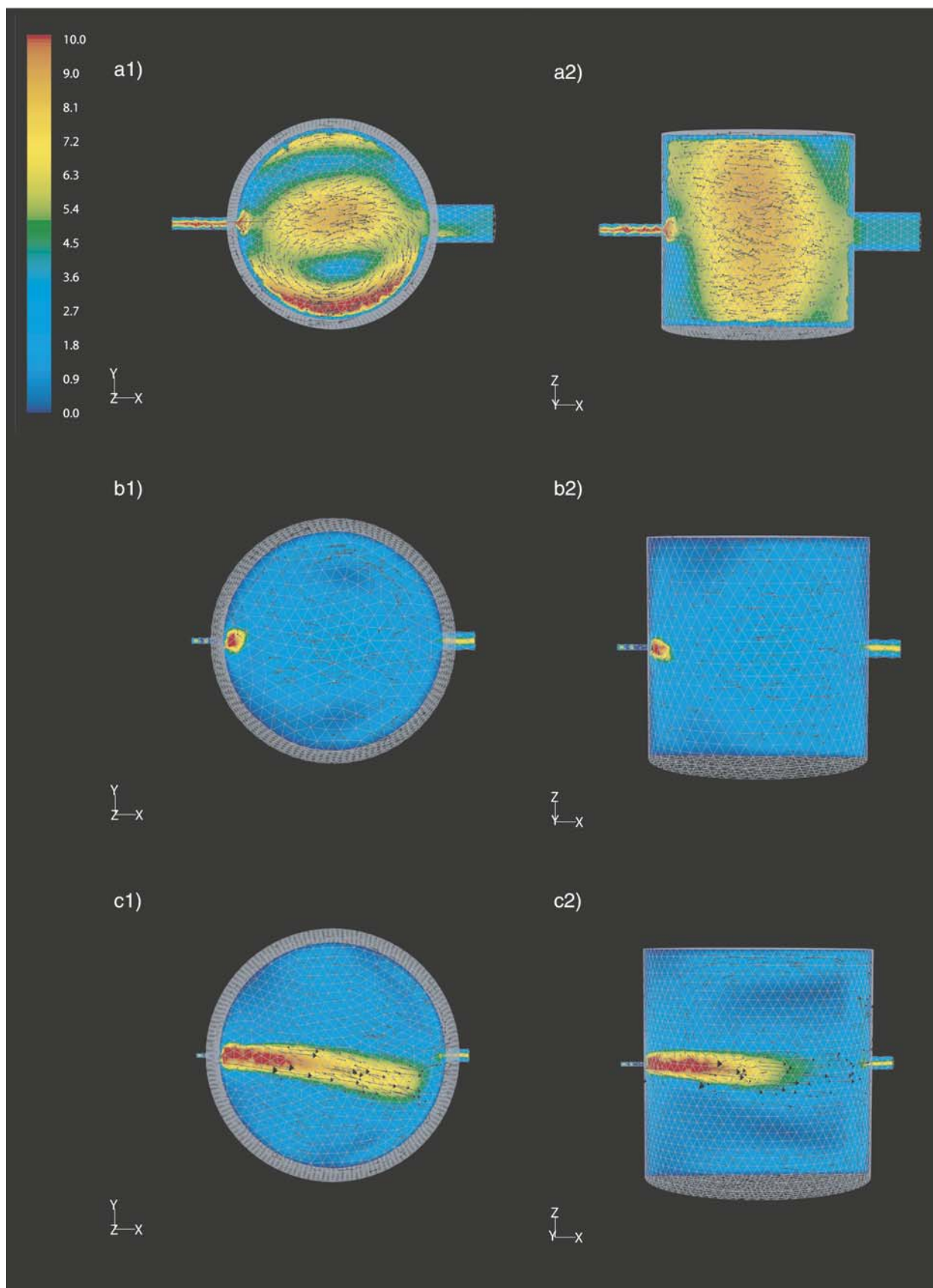


Fig. 1. Top and side view of calculated gas flow velocity (in units of m/s) for 1 L/min Ar inlet flow across cylindrical cells of volume: a) 2.7 cm<sup>3</sup>, b) 33.7 cm<sup>3</sup>, c) 98.2 cm<sup>3</sup>.

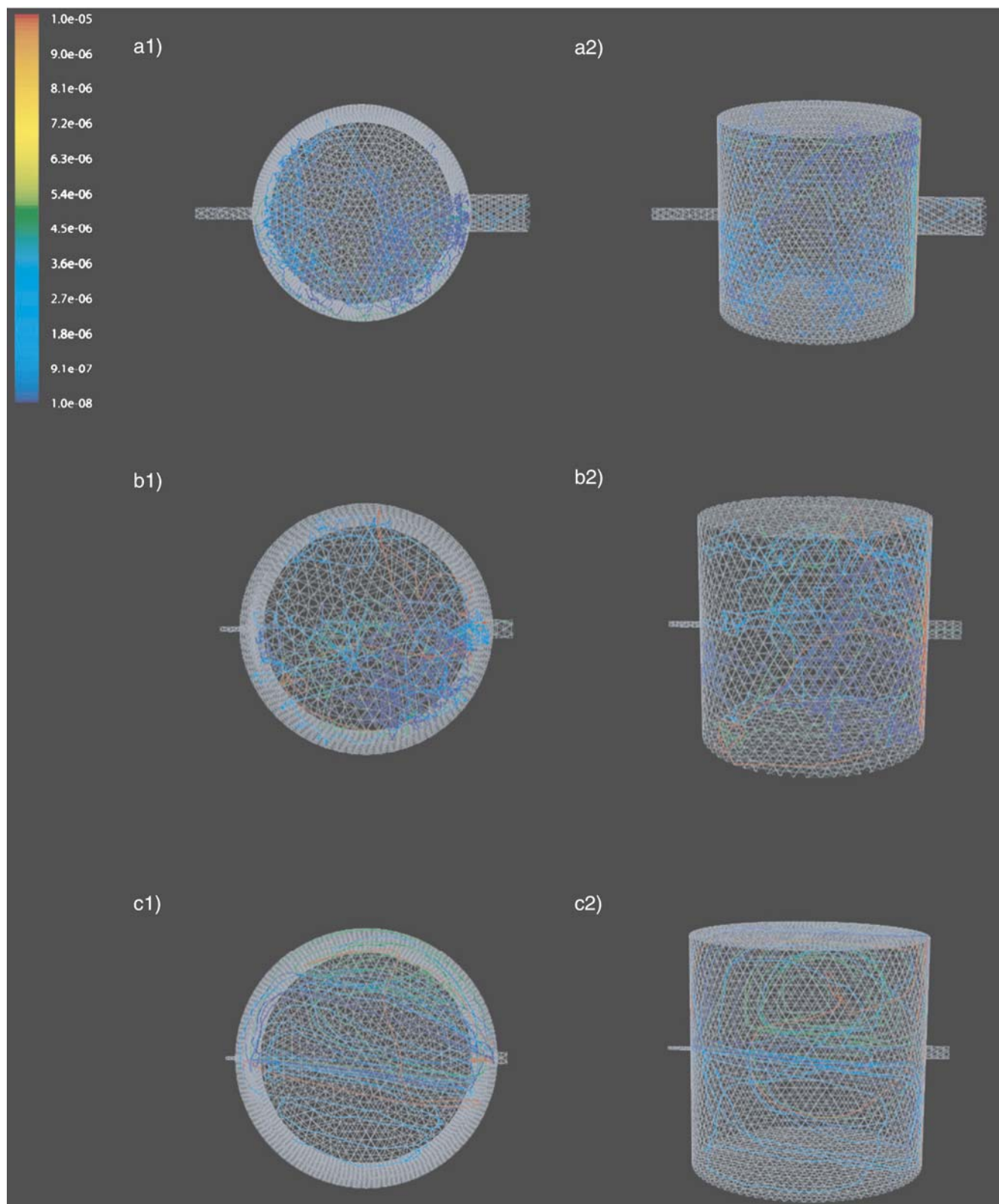


Fig. 2. Top and side view of calculated particle trajectories for different particle sizes (in unit of m) for 1 L/min Ar inlet flow across three cells of volume: a) 2.7 cm<sup>3</sup>, b) 33.7 cm<sup>3</sup>, c) 98.2 cm<sup>3</sup>.

efficiency. On the other hand, coarse particles are heavy, sluggish and prone to gravitational settling, which in certain flow patterns reduces their transport efficiency, too. As a rule of thumb, the most

efficiently extracted fractions are between 0.3 and 3  $\mu\text{m}$ , whereas the transport of ultra-fine or very coarse particles can vary according to the specific flow dynamics.

Fig. 2.a shows the particle trajectories in the 2.7 cm<sup>3</sup> ablation cell. The finer particle sizes are characterized by the typical complex erratic trajectories, which makes these particles more prone to diffuse across the ablation cell volume and follow the gas recirculation. However, the reduced cell volume and the enhanced gas mobility in this kind of cell keep these particles always in motion, with good probability to leave the cell at a certain time. If they accumulate in certain subzones of the cell volume, the chance of aggregation and clustering is enhanced [32]. The coarser fractions have more regular and straight trajectories, which favors prompt collision with the walls. The information in this figure should be combined with the one provided in Fig. 1 to understand that the particle evacuation is a rather stochastic process. This means that the reduced volume cell operates as a *particle stirrer*, and periodically the moving particles meet the outlet gate and are carried into the transport tubing (stochastic extraction). The calculated transport efficiency was here close to 5% (Table 2).

Fig. 2.b shows the particle trajectories in the 33.7 cm<sup>3</sup> ablation cell. Note that the particle trajectories are confined in the forward and bottom region of the ablation cell. Hence, this cell operates as a “particle trap” with size-dependent extraction efficiency. However, due to the visualized trapping at the front zone of the chamber, the calculated extraction efficiency was here higher than above and approx. 10% (see Table 2).

Finally, Fig. 2.c shows the particle trajectories in the 98.2 cm<sup>3</sup> ablation cell. One immediately recognizes, from a comparison to both previous cases, that the trajectories are not so jagged or confused as above, and they follow closed loops departing from the inlet–outlet axis. The gas speed is more modest than in the previous case, which enhances the possibility of permanent loss, due to gravitational settling of large particles. This also suggests that ablated samples would provide a composed signal profile with two components: a sharper component due to the particles in the gas inlet jet that are rapidly extracted, and a more slowly waning component of recirculating particles dispersed laterally. Such a two-slope profile model is best visualized experimentally looking the trace of LA–ICPMS transient signals when using a logarithmic intensity scale. The calculated extraction efficiency for the 98.2 cm<sup>3</sup> ablation cell, as shown in Table 2, was approx. 9%, i.e., comparable to the one obtained for the 30 cm<sup>3</sup> ablation cell. This shows that the increase in extraction efficiency as obtained with large volume cells plateaus for a volume larger than 50 cm<sup>3</sup>. This might be explained with the fact that the particle number density as well as the particle velocity reduce and eventually compensate the effect of a more regular flow pattern that might drive the particle trajectories towards the outlet gate. The reproducibility of the transport efficiency results (uncertainty bars as 1s and  $n=3$ ) is a function of the flow pattern: the more erratic flow pattern in the small volume cell produces a less reproducible set of values (RSD of 4.2% for the 2.7 cm<sup>3</sup> ablation cell) than the more regular flow pattern in the larger cells (2.2% for the 33.7 cm<sup>3</sup> ablation cell and 1.2% for the 98.2 cm<sup>3</sup> ablation cell).

### 3.3. Performance optimization

The strive towards the highest number of particle receding from the ablation cell has several implications for the elemental analysis. First, the *sensitivity*. It is easily understood that the higher the extracted number of particles, the more intense is the resulting analytical signal for the same sample. Second, the potential occurrence of *elemental fractionation*. Since the particle ensemble is compositionally heterogeneous, if the cell would operate as a particle size filter, then the obtained results are not analytically reliable. Third, *cross-contamination*. In fact, all particles that are lost inside the ablation cell might contaminate the setup and interfere with subsequent determinations.

In the following we want to discuss some modifications that might favor an improvement of the sample chamber performance. The analytical figures that might drive a design improvement are essentially two: maximization of *extraction efficiency*, and enhancement of *transport speed*. The latter condition is important to ensure fast rising signal and minimal tailing, which is a requirement in depth-profiling analysis. For clarity we will discuss such modifications on results obtained for a conventional 30 cm<sup>3</sup> ablation cell, which is very familiar to most of LA–ICPMS users.

#### 3.3.1. The design

Firstly, we evaluated the possibility to modify the perimeter of the ablation cell and introduce an aerodynamic design. This means that instead of a circular base, the cell had an elliptical base with the inlet–outlet axis as the geometrical as well as major flow axis. Fig. 3 shows the velocity distribution (a) for such an elliptical cell, shown on a horizontal and a vertical cross-section, together with particle trajectories (b). Close to the inlet, the gas plume extends forward, and slightly upward, due to the onset of a forced vertical convection. The latter pushes the gas forward in the higher regions of the cell volume, and since the forward-moving gas mass is not completely evacuated through the outlet, it flows backward along the bottom of the ablation chamber. Such a rotational regime influences the efficiency of aerosol extraction in a particle size-dependent way, as shown in Fig. 3.b. In fact, only coarse particles because of their higher momentum can keep in the main stream as they float in the inlet plume, whereas the finer particles tend to diffuse across the whole chamber volume. Thus, the fine particles are more prone to depart from the main *extracting flow* and to be re-transported backward in closed looping trajectories. In spite of such a selective flow pattern, the overall extraction efficiency was rather improved by more than a factor of 2 by an elongated design, as shown in Table 2, namely to a value of 25%.

Still remains that despite the significant improvement in efficiency, the elliptical ablation cell showed a limitation concerning the ability to rapidly and quantitatively extract all aerosol fractiles. This situation was partly so because the outlet cross-section was a bottleneck, which induced back-flow along the floor. Unfortunately, the end size of the outlet is limited by the diameter of the transport tubing that connects the ablation cell to the ICP torch. However, it is possible to consider the

possibility to shape the gas outlet with a conical or pyramidal profile. This means that instead of having a hole on the front cell wall, one might obtain a gradual restriction of the cell cross-section at the front until the size of the tubing is attained. One can also expect that this solution would help to support a gradual continuous increase of gas flow velocity towards the outlet, which improves extraction conditions. Calculations were done for an ablation cell with a pyramidal and conical front, which should have mitigated back-flow. The modified front of the cell, obtained from a pyramidal duct joining the sample chamber to the gas outlet, did not produce any relevant modification on the pressure inside the cell. This was, as discussed above for the other designs, homogenous and slightly above atmospheric value. A slightly increasing pressure gradient was found from the gas inlet to the outlet. Such condition was best visualized by the velocity distribution, where the inlet gas plume suddenly stops approx. at the onset of the pyramidal front. Compared to the previous case of Fig. 3, one

could note that the clipping of the peripheral circulation, by stricter confinement of the flow at the front, favors a wider extension of the gas plume. However, the front restriction operates anyway like a bottleneck that impedes the passage of the particles of lower momentum (i.e., the finer ones) near the gas outlet, hence reducing their evacuation probability. The trajectories of the particles showed that the finer fraction is confined in the rear region, whereas the coarser ones have enough momentum to overcome the barrier. In conclusion, the overall calculated extraction efficiency is here reduced from the case of the elliptical ablation cell, down to a value of 10%. However, it is noteworthy to say that this cell design significantly improved the *stability* of the sample introduction with as low as 0.1% RSD of the extraction efficiency.

In conclusion, as far as the design is concerned, one should devise a channel-like cell with a circular cross-section, whose main symmetry axis is parallel to the direction of gas flow. Unfortunately, all present-day commercial *drum* cell designs

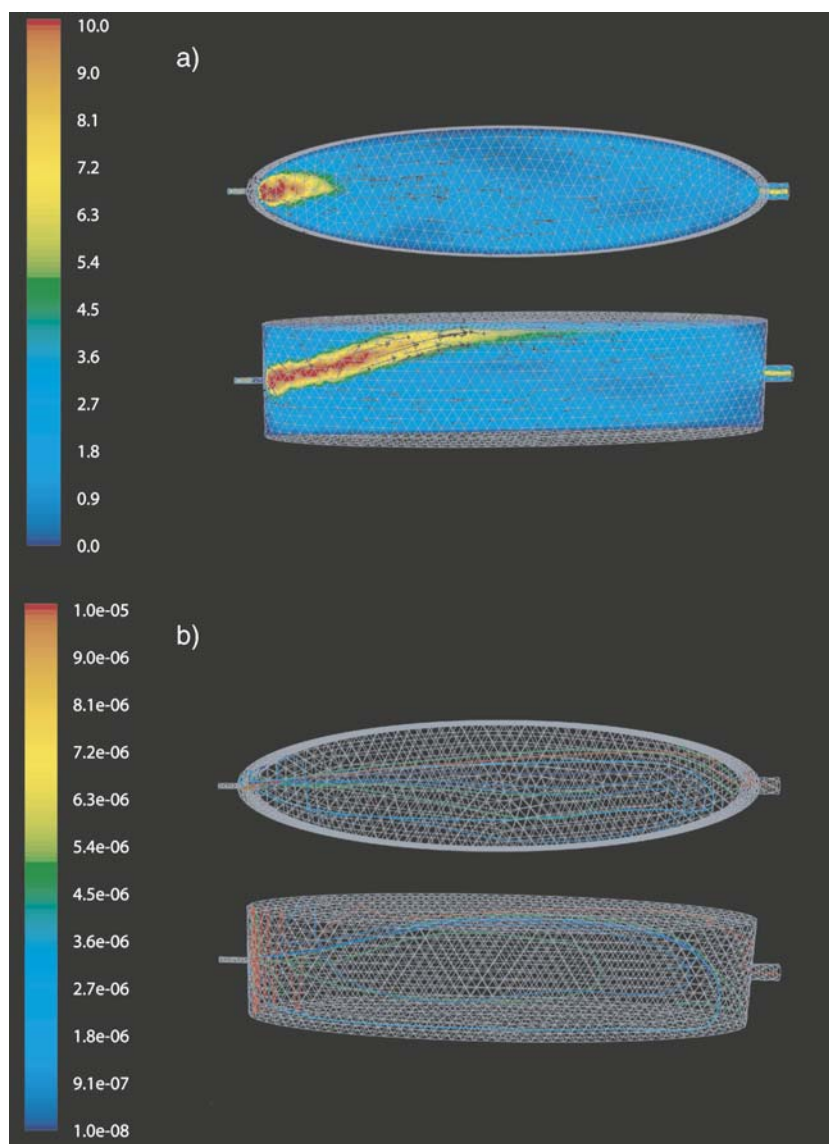


Fig. 3. Top and side view of calculated (a) gas flow velocity (in m/s) and (b) size-dependent (in m) particle trajectory across a 32.1 cm<sup>3</sup> elliptical cell.

exhibit a symmetry axis orthogonal to the gas flow axis, which induces vorticity and re-circulation. Bleiner [23] developed a novel ablation cell design, the ‘piston cell’, realized from a plastic syringe of 50 mL. The flow through such a cell was improved with a plug flow flush, using a patented nozzle device [33]. The simulation results showed that the flow characteristics are axi-symmetric and a plug flow profile is created which explains why the extraction efficiency is factor of 6 higher than the standard chamber designs discussed above. As shown in Table 2 we calculated an extraction efficiency for the piston cell of approx. 66%.

Our study suggests that strategies to force and confine the flow by mere re-design of the ablation cell geometry are important to improve the performance, though they must be matched to the optimization of the fluid-dynamic parameters of the system.

### 3.3.2. The operating conditions

For a given ablation chamber design, the performance of the cell evacuation process is also influenced by two main operating parameters, i.e., the gas flow and the type of carrier gas used. To begin with, the use of one single “point-like” gas inlet has been retained too restrictive to ensure homogeneous sweep across the cell volume and efficient extraction conditions, especially in large volume cells. Fig. 4 shows the obtained results of (a) gas flow velocity and (b) particle trajectories for an ablation cell to which two additional gas inlets were applied at an angle of  $60^\circ$ . The total flow is identical to the one-inlet case, i.e. 1 L/min, though it is here split among the three inlets. The velocity distribution shows a set of gas inlet plumes that more or less homogeneously sweep the rear part of the cell volume. The combination of the three jets supports the forward extension of

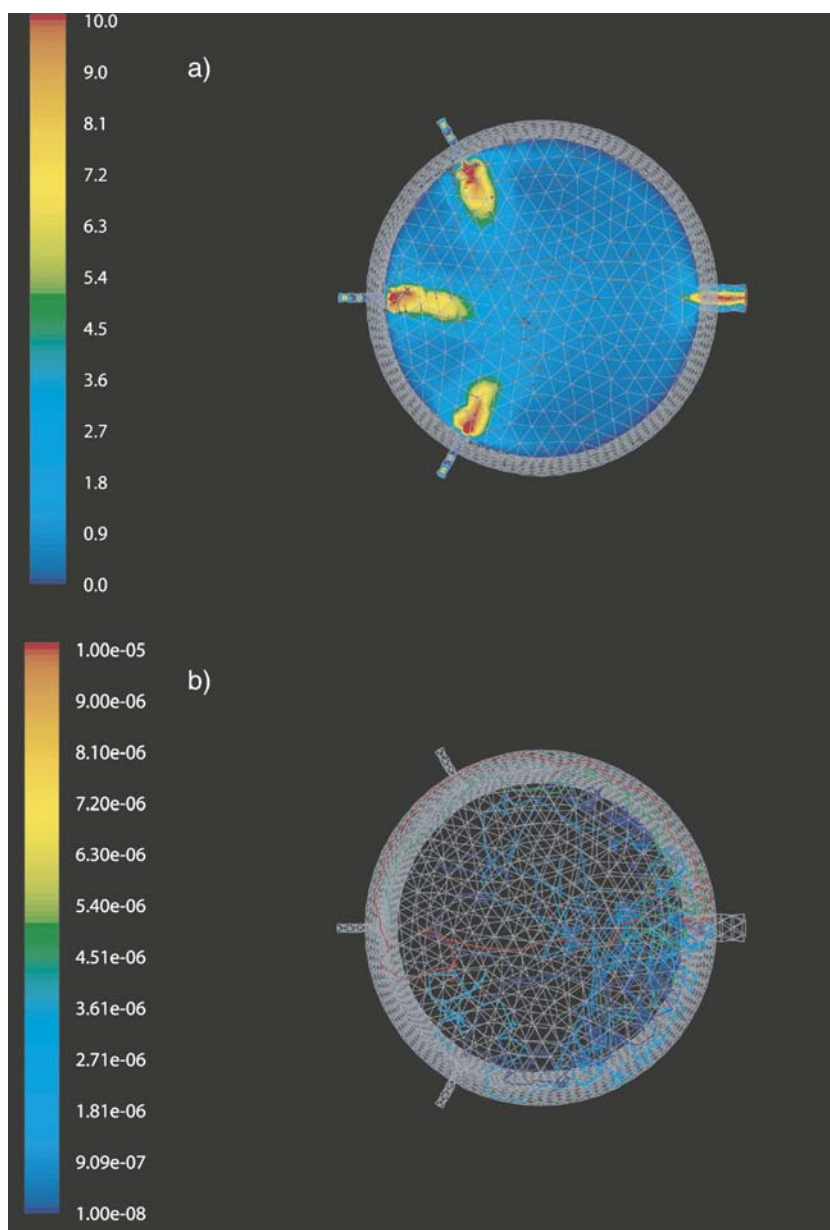


Fig. 4. Calculated (a) gas flow velocity (in m/s) and (b) size-dependent (in m) particle trajectory across a  $33.7 \text{ cm}^3$  cell with three inlets of  $0.33 \text{ L/min}$  flow rate each.

the central gas channel more than in the one-inlet case (Fig. 1.b). However, one should note that the general enhancement of velocity is not significant, especially in the forward region close to the gas outlet. Fig. 4.c summarizes particle trajectories and visualizes that the sweeping of the cell was improved only in the rear region, close to the three inlets. Particles swirl and accumulate in the front regions, which does not improve the extraction efficiency in a significant way. In fact, as also shown in Table 2, the calculated extraction efficiency was approx. 10%.

The standard flow rate value adopted so far was 1 L/min. Fig. 5 summarizes the computational results for 0.1 L/min Ar inlet (a) and for 0.5 L/min (b), with respect to the velocity distribution (left-hand side) and the particle trajectories (right-hand side). For 0.1 L/min Ar flow (shown in a) one notes that

the region of significant gas motion is rather limited to the part close to the gas inlet. The rest of the gas motion is set into a gentle clockwise rotation along the cell walls. In this way, the particles can stochastically leave from the cell when they pass by the gas outlet. As a consequence, the extraction speed is rather poor, and long LA-ICPMS transient signals are presumably obtained. An increase of the gas flow rate to 0.5 L/min (shown in b) is sufficient to improve dramatically the transport conditions, at least along the inlet–outlet axis. Such a flow rate indicates even better performance than the standard case with  $F=1$  L/min, which was possibly too high. At both sides, the already discussed recirculation sub-cells were found. As a direct consequence, the flow through the cell is split into a (larger) high-efficiency area along the inlet–outlet axis (see particles trajectories shown in b2) and a (reduced)

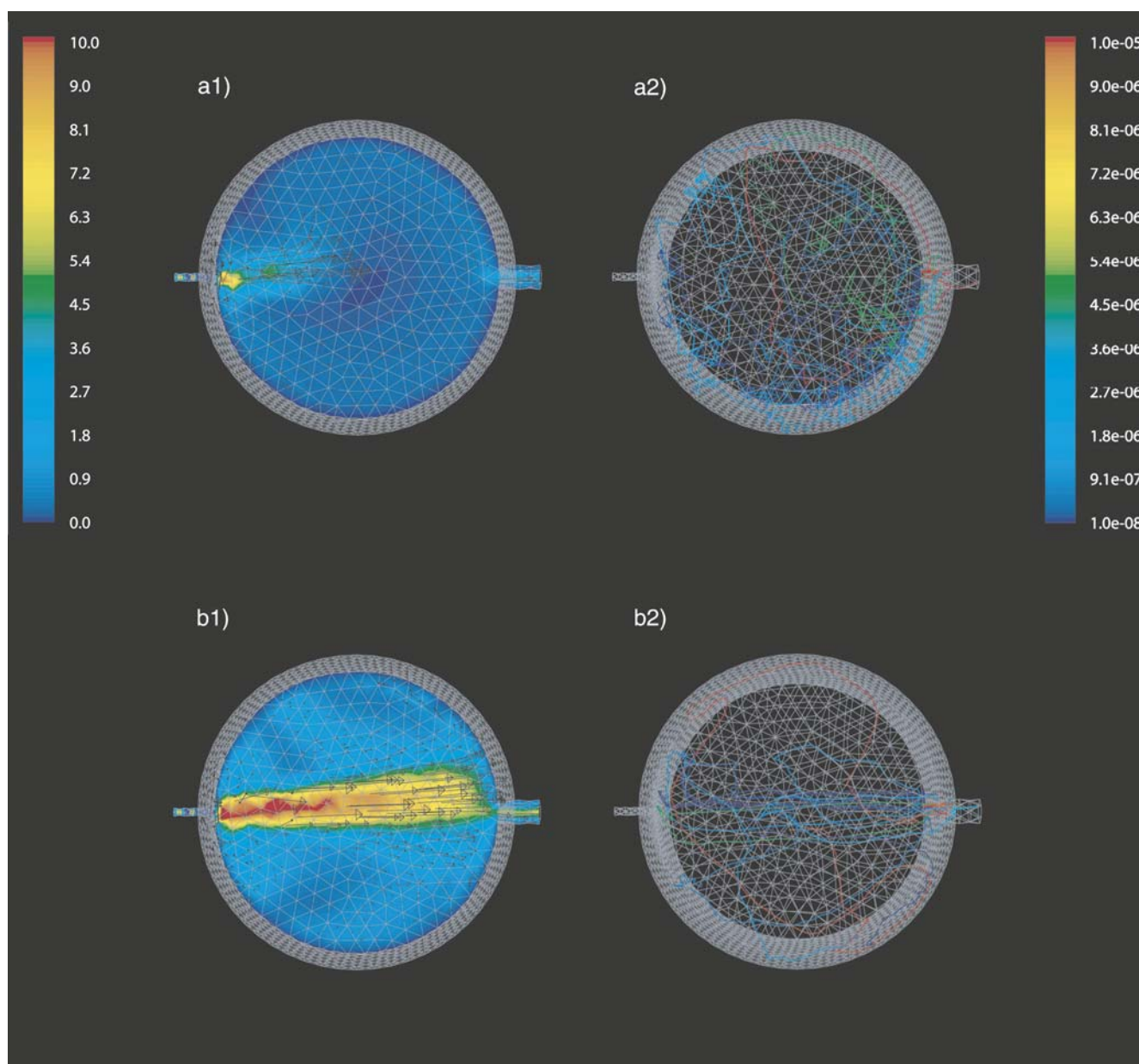


Fig. 5. Calculated gas speed (in m/s, on the left), and size-dependent (in m, on the right) particle trajectories across a 33.7 cm<sup>3</sup> cell with one inlet Ar gas at 0.1 L/min (a) and 0.5 L/min (b).

low-efficiency area at the margins. Hence, one concludes that the improvement of gas inlet distribution and dosing should be combined with a more appropriate particle evacuation principle.

Finally, it is noteworthy to show our computational results obtained using helium (He) instead of Ar as a carrier gas. Briefly, we have to recall that the main physical differences between the two gases are the mass density (for Ar is  $1.7837 \text{ kg/m}^3$ , and for He is  $0.1785 \text{ kg/m}^3$  [34]), which influences their diffusivity according to the Graham law [35], the cross-section (the empirical covalent radius of Ar is 97 pm, and for He is 32 pm [34]), and the mean free path (at atmospheric pressure it is 70 nm for Ar, and almost a factor of three larger for He, i.e. 190 nm). Other physical properties, such as the viscosity are rather similar. The thermal conductivity, which is indeed very different and higher for He, is not considered here to be of relevance for CFD computations, but possibly for the ICP-supported vaporization

of the sample introduced. Fig. 6 summarizes the calculated results for 0.5 L/min He inlet (a) and for 1.0 L/min (b) in the  $33.7 \text{ cm}^3$  cylindrical cell, with respect to the gas velocity distribution (left-hand side) and the particle trajectories (right-hand side). In both velocity distribution plots (a1 and b1) one notes that the central gas plume is much wider than for the case of Ar, as shown above. Interestingly, even in the marginal regions there is no significant back-flow. In fact, even though the speed difference between the center and the boundary can be as high as a factor of 10 in module, almost all velocity vectors point forwards, especially at 1 L/min. Hence, He substantially eliminates the dichotomy of low and high efficiency zoning. The particle trajectories (a2 and b2) show a limited in-cell recirculation, mostly limited to the particle sizes smaller than 100 nm, due to diffusion forces. This effect has to be explained with the larger mean free path of He as compared to Ar, so that the ultra-fine sizes, which are numerically very abundant in LA-

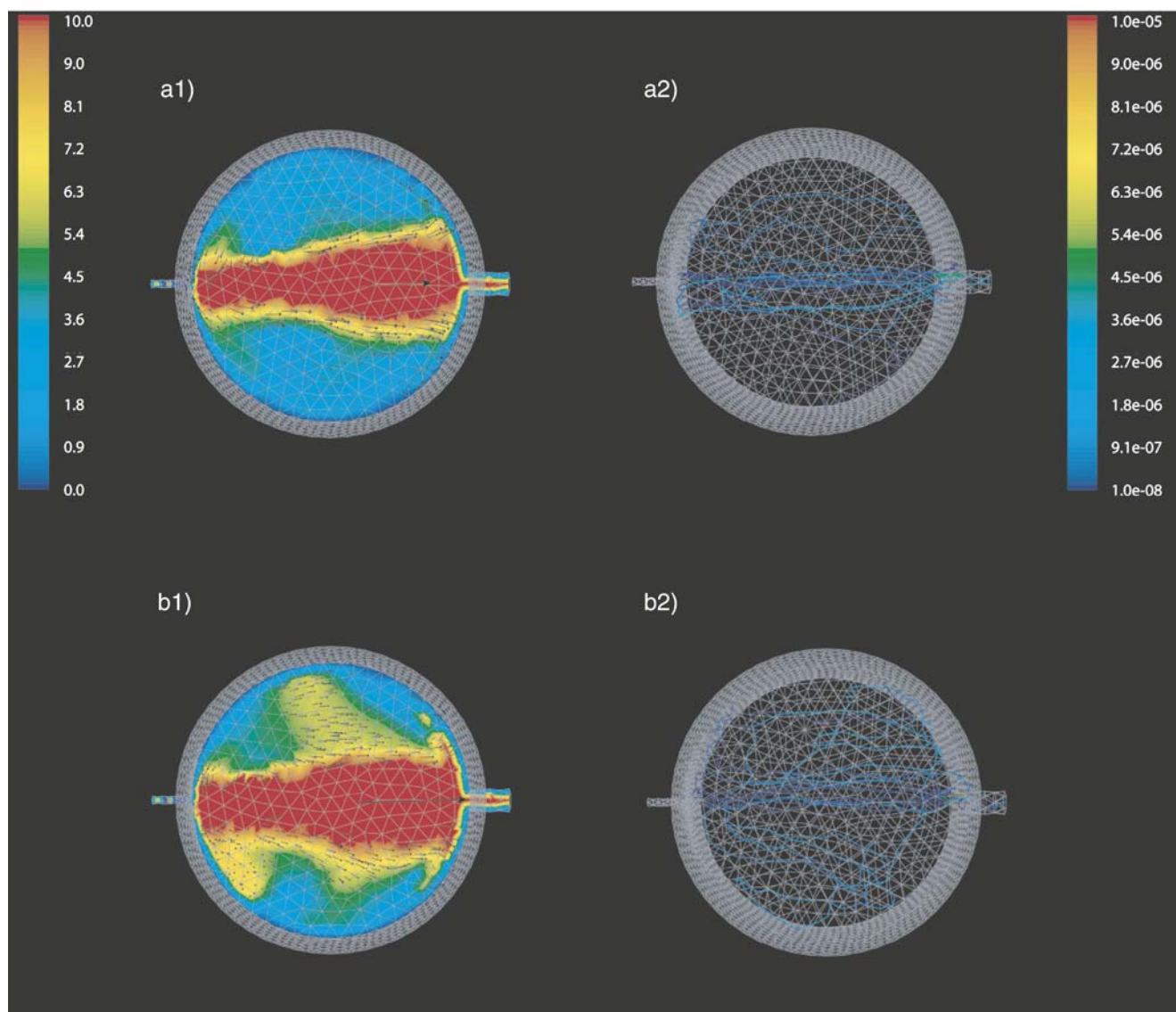


Fig. 6. Calculated gas speed (in m/s, on the left), and size-dependent (in m, on the right) particle trajectories across a  $33.7 \text{ cm}^3$  cell with one inlet Ar gas at 0.5 L/min (a) and 0.1 L/min (b).

induced aerosols, suffer from molecular slipping effects [36]. This physical process also explains the slightly degraded transport efficiency obtained in all ablation cell designs when He is used (see Table 2). However, concerning our discussion on transport speed, the use of He provides faster chamber flush, across the entire cell volume.

#### 4. Conclusions

Computational fluid dynamics (CFD) simulations were carried out to investigate the performance of conventional laser ablation sample chambers, and to improve their capabilities. The study focused on the investigation of two main aspects, i.e., the extraction efficiency of the various designs, as influenced by the flow pattern, and the speed of sample chamber flush.

The extraction efficiency of conventional cylindrical ablation cells was found to be between 5 and 15% depending on the volume, inlet flow rate and type of carrier gas. It should be pointed out that our calculated values refer to a laser-induced aerosol produced by ns-pulse beams. In any case, appropriate changes to the design allowed to obtain up to 66% extraction efficiency, which would greatly improve the analytical figures of merit of LA–ICPMS. In fact, the use of a cylindrical cell whose symmetry axis is not parallel with the gas flow direction has so far caused limited sample extraction. The use of needle gas inlets (*point jet* gas introduction), which guarantees a higher gas injection velocity, was found to destabilize the gas flow pattern, so that in-cell recirculation was extensively found. However, the gas introduction using a plug flow approach (*surface sweep* gas introduction) permitted to avoid in-cell recirculation or trapping, although producing a lower translation speed.

#### Acknowledgments

Financing from the *Fonds Wetenschappelijk Onderzoek – Vlaanderen* (FWO) is acknowledged for supporting my visiting postdoctoral fellowship in the PLASMANT group. I am also grateful to Prof. D. Günther (ETHZ) for the invitation in Zurich at the 2006 European Workshop for Laser Ablation ICP–MS, where this work has been presented as kick-off lecture.

#### References

- [1] C.A. Heinrich, T. Pettke, W.E. Halter, M. Aigner-Torres, A. Audétat, D. Günther, B. Hattendorf, D. Bleiner, M. Guillong, I. Horn, Quantitative multi-element analysis of minerals, fluid and melt inclusions by laser-ablation inductively-coupled-plasma mass-spectrometry, *Geochim. Cosmochim. Acta* 67 (2003) 3473–3497.
- [2] S.F. Durrant, Laser ablation inductively coupled plasma mass spectrometry: achievements, problems, prospects, *J. Anal. At. Spectrom.* 14 (1999) 1385–1403.
- [3] The Merriam–Webster Dictionary, Merriam–Webster, 2003.
- [4] D. Bleiner, F. Belloni, D. Doria, A. Lorusso, V. Nassisi, Overcoming pulse mixing and signal tailing in laser ablation inductively coupled plasma mass spectrometry depth profiling, *J. Anal. At. Spectrom.* 20 (2005) 1337–1343.
- [5] L. Moenke-Blankenburg, H. Moenke, J. Mohr, W. Quillfeldt, K. Wiegand, W. Grassme, W. Schroen, Neue aspekete der gertetechnik und der methodik zur laser-mikro-emissionsanalyse, *Spectrochim. Acta Part B* 30 (1974) 227–234.
- [6] L. Moenke-Blankenburg, Laser-inductively coupled plasma spectrometry, *Spectrochim. Acta Rev.* 15 (1993) 1–37.
- [7] M. Gaeckle, D. Günther, PhD thesis, Universitaet Halle-Wittenberg, 1990.
- [8] D. Bleiner, D. Günther, Theoretical description and experimental observation of aerosol transport processes in laser ablation inductively coupled plasma mass spectrometry, *J. Anal. At. Spectrom.* 16 (2001) 449–456.
- [9] L. Fodor, P. Pungor, E. Kantor, T. Polos, Atomic absorption spectrometry of laser-nebulized samples, *Talanta* 23 (1976) 585–586.
- [10] F. Leis, K. Laqua, Emissionsspektralanalyse mit anregung des durch laserstrahlung erzeugten dampfes fester proben in einer mikrowellenentladung. grundlagen der methode und experimentelle verwirklichung, *Spectrochim. Acta Part B* 33 (1978) 727–740.
- [11] W. Carr, G. Horlick, Laser vaporization of solid metal samples into an inductively coupled plasma, *Spectrochim. Acta Part B* 37 (1982) 1–15.
- [12] T. Ishizuka, Y. Uwamino, Inductively coupled plasma emission spectrometry of solid samples by laser ablation, *Spectrochim. Acta Part B* 38 (1983) 519–527.
- [13] M. Thompson, J.E. Goulter, F. Sieper, Laser ablation for the introduction of solid samples into an inductively coupled plasma for atomic-emission spectrometry, *Analyst* 106 (1981) 32–39.
- [14] K. Dittrich, R. Wennrich, Atomabsorptionsspektrometrie durch laserverdampfung mit nachfolgender elektrothermischer atomisierung, *Spectrochim. Acta Part B* 35 (1980) 731–740.
- [15] A. Gray, Solid sample introduction by laser ablation for inductively coupled plasma source mass spectrometry, *Analyst* 5 (1985) 551–556.
- [16] P.G. Mitchell, J. Sneddon, L.J. Radziemski, A sample chamber for solid analysis by laser ablation/DCP spectrometry, *Appl. Spectrosc.* 40 (1986) 274–275.
- [17] P. Arrowsmith, Laser ablation of solids for elemental analysis by inductively coupled plasma mass spectrometry, *Anal. Chem.* 59 (1987) 1437–1444.
- [18] T.D. Bennett, C.P. Grigoropoulos, D.J. Krajnovich, Near-threshold laser sputtering of gold, *J. Appl. Phys.* 77 (1995) 849–864.
- [19] P. Arrowsmith, S.K. Hughes, Entrainment and transport of laser ablated plumes for subsequent elemental analysis, *Appl. Spectrosc.* 42 (1988) 1231–1239.
- [20] C.C. Garcia, H. Lindner, K. Niemax, Transport efficiency in femtosecond laser ablation inductively coupled plasma mass spectrometry applying ablation cells with short and long washout times, *Spectrochim. Acta, Part B* 62 (2007) 13–19.
- [21] G.H. Su, S.L. Lin, Studies on the complete laser vaporisation of powdered solid samples into an inductively coupled plasma for atomic emission spectrometry, *J. Anal. At. Spectrom.* 3 (1988) 841–847.
- [22] H.R. Cousin, B. Magyar, Precision and accuracy of Laser Ablation–ICP–MS analysis of rare earth elements with external calibration, *Mikrochim. Acta* 113 (1994) 313–323.
- [23] D. Bleiner, PhD thesis, ETH Zurich, 2002.
- [24] G.M. Hieftje, J.H. Barnes IV, O. Groen, A.M. Leach, D. McClenathan, S.J. Ray, D. Solyom, W.C. Wetzel, M. Bonner-Denton, D. Koppelaar, Evolution and revolution in instrumentation for plasma-source mass spectrometry, *Pure Appl. Chem.* 73 (2001) 1579–1588.
- [25] J. Pisonero, D. Fliegel, D. Günther, High efficiency aerosol dispersion cell for Laser Ablation–ICP–MS, *J. Anal. At. Spectrom.* 21 (2006) 922–931.
- [26] D. Bleiner, A. Bogaerts, Computer simulations of laser ablation sample introduction for plasma-source elemental microanalysis, *J. Anal. At. Spectrom.* 21 (2006) 1161–1174.
- [27] F.H. Harlow, P.I. Nakayama, Turbulence transport equations, *Phys. Fluids* 10 (1967) 2323–2332.
- [28] B.E. Launder, D.B. Spalding, The numerical computation of turbulent flows, *Comput. Methods Appl. Mech. Eng.* 3 (1974) 269–289.
- [29] D. Bleiner, A. Bogaerts, Multiplicity and contiguity of ablation mechanisms in laser-assisted analytical micro-sampling, *Spectrochim. Acta Part B* 61 (2006) 421–432.
- [30] D. Bleiner, Z. Chen, D. Autrique, A. Bogaerts, Role of laser-induced melting and vaporization of metals during ICP–MS and LIBS analysis, investigated with computer simulations and experiments, *J. Anal. At. Spectrom.* 21 (2006) 910–921.

- [31] R.B. Bird, W.E. Stewart, E.W. Lightfoot, *Transport Phenomena*, Wiley, 2001.
- [32] D. Bleiner, Ph. Gasser, Structural features of laser ablation particulate from Si target, as revealed by FIB technology, *Appl. Phys., A* 79 (2004) 1019–1021.
- [33] D. Bleiner, H. Altorfer, A novel gas inlet system for improved aerosol entrainment in laser ablation inductively coupled plasma mass spectrometry, *J. Anal. At. Spectrom.* 20 (2005) 754–756.
- [34] D.R. Lide (Ed.), *CRC Handbook of Chemistry and Physics*, 83rd edition, CRC, Boca Raton, 2002.
- [35] P.W. Atkins, W. Locke, *Physical Chemistry*, Oxford University Press, 2002.
- [36] P. Baron, K. Willeke (Eds.), *Aerosol Measurement: Principles, Techniques, and Applications*, Wiley–Interscience, 2001.